SuperFocus enables whole-slide cell-level spatial omics from spot-based measurements and histology across modalities

Yao Lu[1], Archibald Enninful[1], Shuozhen Bao[2], Zhiliang Bai[3], Mina L. Xu[4], Yang Xiao[5,6,7†], Rong Fan[1,4,8,9†], and Zongming Ma[10,11,†]

[1]Department of Biomedical Engineering, Yale University, New Haven, CT, United States
[2]Department of Gene Technology, KTH Royal Institute of Technology, Science for Life Laboratory, Solna, Sweden
[3]Department of Biological Engineering, Massachusetts Institute of Technology, Cambridge, MA, United States
[4]Department of Pathology, Yale School of Medicine, New Haven, CT, United States
[5]Department of Pathology, University of Michigan Medical School, Ann Arbor, MI, United States
[6]Department of Computational Medicine and Bioinformatics, University of Michigan Medical School, Ann Arbor, MI, United States
[7]Department of Biomedical Engineering, University of Michigan, Ann Arbor, MI, United States
[8]Yale Stem Cell Center and Yale Cancer Center, Yale School of Medicine, New Haven, CT, United States
[9]Human and Translational Immunology Program, Yale School of Medicine, New Haven, CT, United States
[10]Department of Statistics and Data Science, Yale University, New Haven, CT, United States
[11]Wu Tsai Institute, Yale University, New Haven, CT, United States
[†]Senior Authors

Abstract: Spatial omics data acquisition is constrained by an inherent trilemma: balancing experimental cost, spatial resolution, and profiling scope (in terms of both plexity and field of view). Currently, spot-based technologies coupled with histological images represent one of the most scalable solutions, yet they lack single-cell precision and are often limited in field of view for omics. Here, we introduce SuperFocus, an AI-powered framework that predicts omics features with high fidelity for individual cells across whole-slide images from spot-level omics data acquired on the same or adjacent slides. It substantially relaxes the trilemma by achieving single-cell resolution and whole-slide field of view without increasing experimental cost or sacrificing plexity. SuperFocus implements a novel constrained cascading imputation scheme to minimize hallucination and outputs two per-feature quality-control scores that flag potentially unreliable predictions for each feature. When predicting for cells outside the profiled field of view, SuperFocus additionally provides a prediction-credibility score for each cell that prevents overconfidence when relevant histological patterns are undersampled or absent from the training data. We validate the fidelity of SuperFocus by benchmarking against multiple ground-truth single-cell and subcellular resolution spatial datasets across different platforms, demonstrating highly concordant cell-level feature recovery. We evaluate SuperFocus on both spatial transcriptomics and spatial epigenomics modalities and observe consistent performance over diverse platforms, tissues, and conditions. We demonstrate its utility by resolving the MALT lymphoma microenvironment at single-cell resolution using spot-level Patho-DBiT data, and by performing single-cell resolution motif analysis of the human hippocampus using spot-level spatial ATAC-seq. Overall, SuperFocus provides an effective *in silico* solution to the spatial omics trilemma, empowering single-cell-resolved spatial analysis from standard spot-level inputs and histological images.

Artificial intelligence | Data integration | H&E | Spatial ATAC-seq | Spatial transcriptomics

Correspondence: ***yangxa@umich.edu, rong.fan@yale.edu, zongming.ma@yale.edu***

Introduction

Spatially resolved molecular technologies have become indispensable for dissecting biological organization and disease heterogeneity *in situ* (1–7). In principle, spatial omics can map cellular organization and interactions in intact tissue, capturing the rich spatial context that dissociated single-cell assays eliminate. In reality, data acquisition faces an inherent trilemma: experimental cost, spatial resolution, and profiling scope (panel plexity and field of view) cannot be simultaneously optimized (8, 9). Spot-based platforms such as Visium (10), DBiT-seq (11), and Spatial ATAC-seq (12) strike a scalable compromise, offering cost-effective, high-dimensional molecular readouts. Yet, their spot-level measurements limit spatial resolution, blur single-cell details, and constrain omics field of view.

By carefully examining histological images, pathologists can diagnose disease, delineate lesions, and often recognize key cell types and tissue structures. These judgments draw on complementary cues from cell morphology and the surrounding microenvironment. Accordingly, the paired histological image in spot-based spatial assays provides a synergistic resource for computational refinement of spot-level molecular readouts toward higher spatial resolution. Concretely, one can extract morphology features via digital pathology encoders (13–15) and foundation models (16–20) and integrate them with spot-level profiles to sharpen spatial maps (21–23). Despite the progress, several critical limitations hinder reliable generation of cell-level spatial omics details. First, the effective spatial resolution after refinement oftentimes falls short of robust single-cell granularity. In addition, computational "hallucinations" such as artifactual spatial patterns can arise without reliable in-sample diagnostic metrics to flag them. Finally, and increasingly more importantly, the entire paradigm remains confined to spatially resolved transcriptomics, lacking method development and validation for other critical modalities such as spatial epigenomics.

To overcome these limitations, we developed SuperFocus, an AI-powered and adaptable method that accurately predicts high-dimensional molecular features for individual cells over whole-slide images from spot-level measurements and accompanying histological images. SuperFocus is designed to be modality-agnostic, and we have applied it successfully on both spot-based spatial transcriptomics and spatial ATAC-seq datasets. It employs a novel constrained cascading imputation strategy to maintain prediction accuracy across different resolution levels and thus achieves truly single-cell spatial resolution. In addition, we developed two in-sample diagnostic metrics that flag potential global and local deviation in prediction fidelity for each omics feature. Furthermore, to prevent overconfidence when predicting outside profiled field of view, we introduced a prediction-credibility score for each cell where higher scores correspond to more extrapolative predictions by SuperFocus. Overall, SuperFocus addresses the spatial omics data trilemma by retaining cost and data plexity, while achieving single-cell spatial resolution and whole-slide coverage.

We systematically benchmarked SuperFocus against single-cell and subcellular resolution ground-truth spatial transcriptomics datasets across different tissue types and biological conditions. SuperFocus consistently achieved superior performance in molecular feature prediction, cell-type identification, and microenvironment delineation. The proposed in-sample diagnostic metrics and prediction-credibility score showed high sensitivity and specificity, correlated strongly with ground-truth-based validation metrics, and objectively reflect the fidelity of SuperFocus prediction at the granularity of individual features and individual cells, respectively.

We further illustrated the analyses enabled by SuperFocus with two applications. First, in a human MALT lymphoma Patho-DBiT dataset (24), we showed that SuperFocus-predicted single-cell transcriptomic profiles unveiled heterogeneous cell compositions and cell-cell interaction patterns across distinct local tumor microenvironments within a single tissue section. Second, in a human hippocampus co-mapping dataset (25), SuperFocus inferred chromatin accessibility peak profiles for individual cells from spot-level spatial ATAC-seq. These predictions were validated by immunohistochemistry performed on adjacent slides and by independently derived single-cell gene expression profiles on the same slide. The predicted peak profiles enabled the study of transcription factor binding variability across individual cells at the tissue level. Moreover, SuperFocus offered spatially resolved maps of regulatory gene network activity. We have implemented SuperFocus as a Python package which is available at https://github.com/yaolu53/SuperFocus.

Results

Cascading imputation and whole-slide cell-level prediction for spot-based spatial omics modalities. We first provide an overview of SuperFocus (**Super**-resolution re**f**inement of spatial **o**mics data with **c**ascading imp**u**tation and whole-**s**lide cell-level prediction).

The raw input data to SuperFocus includes two parts (**Fig. 1A**): (1) a high-resolution (20X or 40X) digitized histological (H&E) image of a tissue section, and (2) spatially resolved omics measurements at spot level on the imaged section (or on an adjacent section). Here, the omics measurements are possibly only within some relatively small but representative region(s) of the section. For example, the digitized H&E image could be obtained from whole slide imaging with 40X magnification and the spot-level omics data is obtained from applying some spatial omics technology (e.g., Visium, Spatial ATAC-seq) on a selected region of interest (ROI) or multiple ROIs. We impose a common Cartesian coordinate system to align the histological image and the omics spots. Note that the SuperFocus approach we are to describe is modality agnostic. It can be deployed when the omics measurement is transcriptomics, epigenomics, proteomics, multi-omics, etc.

In Stage 1 of SuperFocus, we apply a state-of-the-art vision-transformer based computational pathology model, CellViT (26), to segment cells and to encode cell morphological information provided by the histological image (**Fig. 1A**). We then reduce the dimensionality of the initial single-cell level image encoding by singular value decomposition. We partition each omics measurement spot in a dyadic fashion recursively. We call the spatial resolution of the initial measurement spot the original resolution, and call the original spots resolution-level-0 spots. In each round of partitioning, we obtain subspots of finer spatial resolution, and we call these subspots resolution-level-ℓ subspots where ℓ is the counter of partitioning round. We stop the recursive process when most subspots contain only one cell. We then compute image encoding vectors for each (sub)spot at each resolution level thus created by aggregating the encoding of individuals cells within the (sub)spot and the immediately surrounding (sub)spots at the same resolution level. Moreover, we count the number of cells within each (sub)spot at each resolution level. For omics data, we apply the standard pre-processing suitable for the omics modality. See Materials & Methods for additional details.

In Stage 2 of SuperFocus, we define a cascade of predictive models, one for each resolution level (**Fig. 1B**). At each resolution level, the goal of the corresponding predictive model is to predict the average single-cell level omics expression of each (sub)spot at that resolution level using the (sub)spot's image encoding vector. The deep neural network architectures of these predictive models are intentionally designed to be comparable to facilitate transfer learning (27) across resolution levels. Starting at level 0 (i.e., the original omics spot resolution), we train the cascade of predictive models recursively, with learned parameters of the previous level model serving as a warm start of the training process of the current model. For the precise definition of these models and the tuning parameters used in training them, see Materials & Methods.

To evaluate the capacity of the trained model for predicting individual features, we conclude Stage 2 of SuperFocus by computing two in-sample diagnostic metrics for each omics

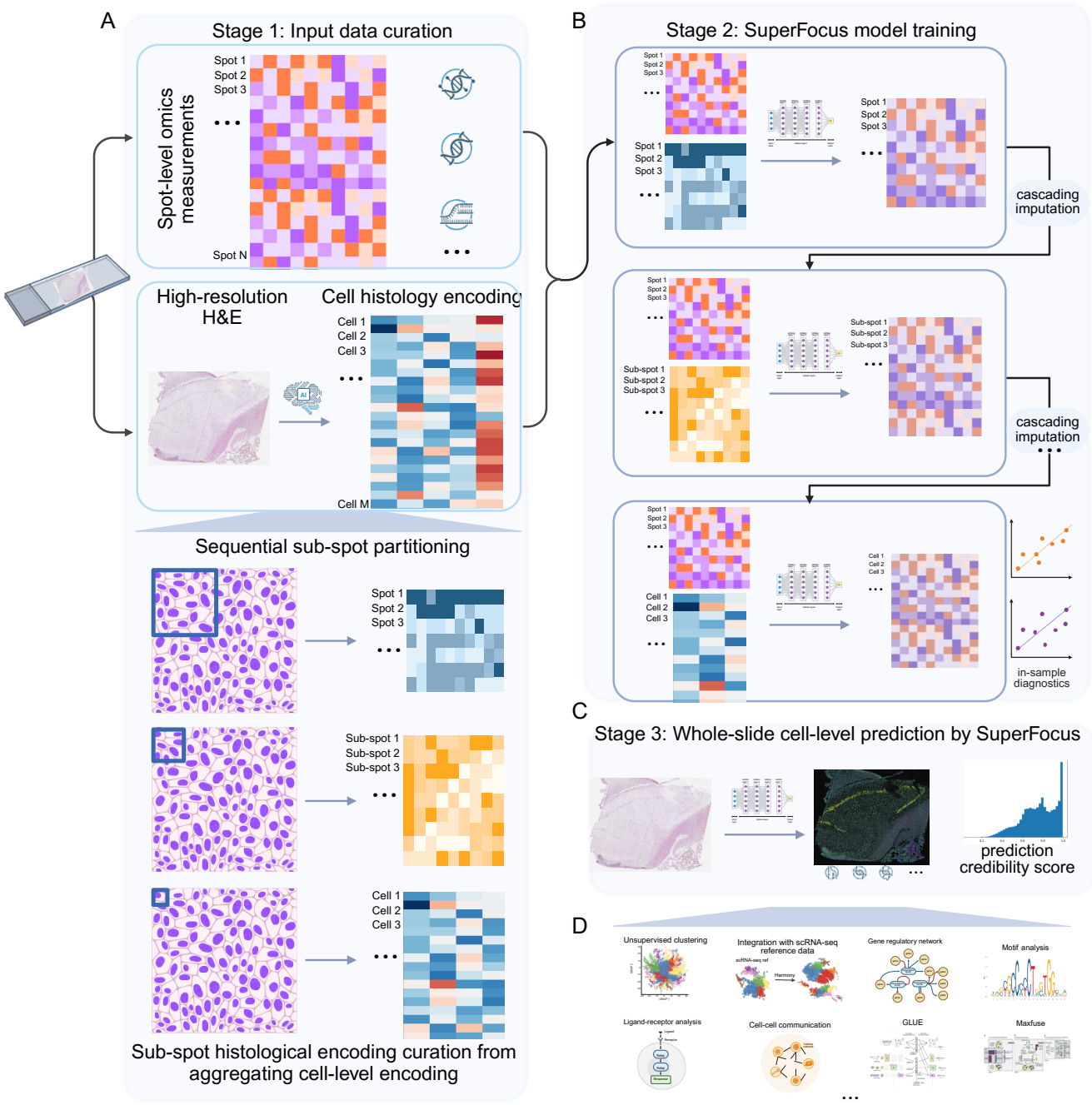

Figure 1: Overview of the SuperFocus pipeline. SuperFocus enables whole-slide cell-level inference from spot-level omics measurements in various modalities, such as Visium, DBiT-seq and spatial-ATAC-seq, by integrating information from an accompanying histological image. **(A)** In Stage 1 of SuperFocus, CellViT segments cells and encodes histology information for individual cells on the H&E image. SuperFocus curates spot-, sub-spot and cell-level features across different resolution levels that are suitable for predicting omics expressions. **(B)** In Stage 2, SuperFocus trains a sequence of deep-neural-net prediction models at increasing finer resolution levels via constrained cascading imputation, starting with the original spot level and ending with single-cell resolution level. In-sample diagnostic metrics can be computed to assess the performance of the trained SuperFocus model at predicting individual omcis features. **(C)** In Stage 3, SuperFocus predicts cell-level expression profiles for the whole slide. prediction-credibility scores for cells outside profiled FOV help minimize hallucination and identify regions with high and low prediction-credibility. **(D)** SuperFocus-predicted cell-level expression profiles empower a wide range of downstream analyses with cell-level resolution and spatial context.

feature. We aggregate the predicted features levels by the trained finest resolution model across all finest resolution subspots in each original observation spot, compute its difference from the observed feature value at the original spot which we call aggregated prediction error of the spot, and collect all the aggregated errors into a long vector whose length equals the number of original spots. The first metric (RSSE) is the ratio of the sum of squared aggregated errors over the sum of squared observed values across original spots, which reflects the global in-sample prediction errors made by the finest resolution model. Higher RSSE values mean worse overall predictions. The second metric (ESL) is the ratio of the ℓ_2 norm of this vector over its ℓ_1 norm, which measures the error spatial locality. Higher ESL values mean more spatially concentrated prediction error patterns. If the trained model predicts a feature well, both metrics should be low for that feature. As both metrics are unit-free, they can also be used to compare prediction accuracy across different features. We note that both metrics are in-sample, i.e., their evaluations only require the training data.

Stage 3 of SuperFocus leverages the trained model at the finest resolution (i.e., the resolution level at which most subspots contain one cell) to predict omics features for all individual cells over the entire imaged tissue section (**Fig. 1C**). To this end, for each cell, we first create a 3-by-3 array of subspots of the same size as the finest resolution ones, with the central subspot centered at the cell center. Next, we compute the image encoding of the central subspot which aggregates all image encoding vectors of all cells intersecting with the 3-by-3 array of subspots, which serves as the input to the trained finest-resolution model. Finally, we use the resulting output of the trained finest-resolution model as the predicted omics features of the cell. We repeat the foregoing process for all cells to generate single-cell omics features over the whole slide. If we are interested in an intermediate resolution level, say resolution level ℓ, we partition the entire image into a grid of subspots of the corresponding size, compute the image encoding of each subspot, and use it as input to the trained resolution-level-ℓ model to impute the average omics expression of each subspot. We obtain the cumulative omics expression of each subspot by further multiplying the model output with the number of cells in each subspot. For each cell predicted, we further assign it a prediction-credibility score that is defined as the reciprocal of the average distance of its image encoding to its k-nearest neighbors in the collection of all image encoding patterns used in training the model at the finest resolution. A low prediction-credibility score for a cell suggests that the histological patterns around the cell is undersampled or absent from the training data, and hence one should not be overly confident in its predicted omics profile.

The SuperFocus-predicted omics features for individual cells over the whole slide empowers a wide range of downstream tasks (**Fig. 1D**). For example, we can annotate individual cells by clustering the predicted omics profiles or by label transfer after integrating with a single-cell reference dataset of the same modality when available. We can also annotate spatial niches/neighborhoods at high granularity with these *in silico* spatial single-cell data. In addition, leveraging both spatial proximity and omics features at single-cell resolution, we can study ligand-receptor type cell-cell interaction or other types of cell-cell communications. When the original spot-level measurements provide epigenomics information, we can perform spatial motif analysis at single-cell granularity over the whole slide. Other potential downstream tasks empowered by SuperFocus include, but are not limited to, (1) cross-resolution cross-modality integration of spatial omics data on the same tissue section or adjacent sections, e.g., the single-cell granularity integration of spot-level spatial transcriptomics data and single-cell spatial protein data generated by DBiTplus (28); (2) cross-modality integration of spot-level spatial omics data with single-cell reference dataset in a different modality, e.g., the single-cell level integration of spot-level spatial transcriptomics data and reference scATAC-seq data by applying some diagonal integration method (e.g., (29, 30)) on the predicted spatial single-cell transcriptomics and the reference scATAC-seq data; and (3) 3D reconstruction of tissue volume with single-cell level molecular details via H&E images of serial sections and relatively sparsely sampled spot-level spatial omics data.

Benchmarking on a paired Visium–Xenium breast cancer dataset. We first benchmarked SuperFocus on a human breast cancer tissue Visium dataset (31) and compared the cell-level prediction results against a Xenium dataset measured on an adjacent section. The two sections were first aligned by STalign (32) and the H&E image of the Xenium section was used in both SuperFocus training and prediction. The SuperFocus model was first trained on the Visium section. The trained SuperFocus model at the finest resolution level was subsequently applied on the Xenium section to predict gene expression profiles for all cells on this section (**Fig. 2A**). We compared the SuperFocus-predicted single-cell gene expressions to the Xenium measurements that served as the ground truth on this section.

For individual transcripts, the predicted expression levels for individual cells by SuperFocus exhibited congruent spatial patterns to the measured levels by Xenium. For example, the transcripts *ERBB2* and *TACSTD2* were highly expressed in tumor regions, *IL7R* highlighted peripheral-tumor regions where immune cells were present, and *ACTA2*, a marker for myoepithelial cells, were enriched surrounding the secretory acini and the ducts, with their Xenium measurements and SuperFocus predictions exhibiting high levels of agreements (**Fig. 2B, Supplementary Fig. 1**). To quantitatively compare spatial similarities between SuperFocus-predicted gene expression levels and the Xenium measurements, we computed the Multi-Scale Structural Similarity (33) (MS-SSIM, precise definition in Materials & Methods) scores for all Xenium-measured genes, where for each gene, a higher MS-SSIM score indicates better prediction, with 1 being the highest possible score. SuperFocus achieved MS-SSIM scores larger than 0.93 for all genes (**Fig. 2E**), with mean 0.97 and standard deviation 0.01, demonstrating the high fidelity of SuperFocus prediction at individual gene level.

In addition, we processed and clustered the SuperFocus-

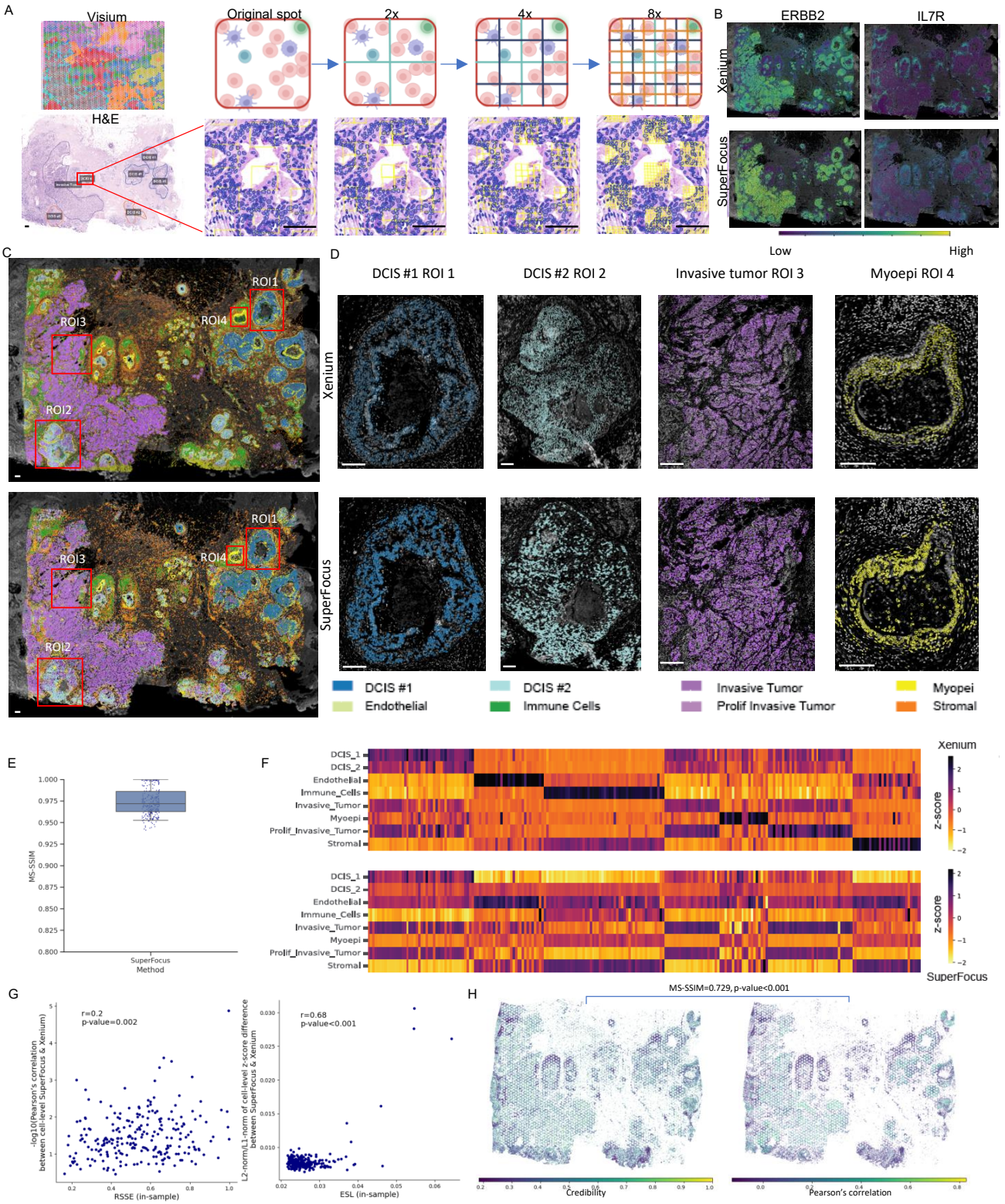

Figure 2: Benchmarking SuperFocus on a paired Visium-Xenium breast cancer dataset. (A) A schematic diagram of SuperFocus training on the Visium breast cancer data, original spot size: 55 μm. **(B)** Spatial plots of SuperFocus-predicted single-cell level marker gene expressions: *ERBB2* (top) and *IL7R* (bottom). **(C)** Cell type annotations based on Xenium-measured (top) and SuperFocus-predicted (bottom) single-cell level spatial transcriptome show consistence. **(D)** Spatial plots of representative cell types at four regions of interest (see **(C)** for their locations on the tissue section) are compared between Xenium (top) and SuperFocus prediction (bottom); **(E)** The boxplot of MS-SSIM scores quantifies similarity between SuperFocus-predicted expressions of Xenium-panel genes and ground-truth Xenium data. **(F)** The heatmaps of gene expression profiles across cell types show similar patterns between SuperFocus prediction and Xenium. **(G)** Plots of feature level in-sample diagnostic metrics RSSE and ELS vs. true single-cell resolution prediction error metrics on overall prediction error and error spatial locality, respectively, show statistical significant correlations. **(H)** Spatial plot of cell-level prediction-credibility scores demonstrates high concordance with spatial plot of true prediction accuracy, successfully flagging regions of extrapolative SuperFocus prediction and avoiding overconfidence. Scale bar: 100 μm.

predicted single-cell gene expression profiles following a standard clustering pipeline for scRNA-seq data. Subsequently, we identified a comparable set of cell types (i.e., Leiden clusters) from the SuperFocus predictions to the original annotations in (31). The spatial distributions of SuperFocus and Xenium cell type annotations were well aligned (**Fig. 2C**). Further zooming in, as shown in the left two columns of **Fig. 2D** (ROIs #1 and #2), we found that the regions enriched with two types of DCIS by SuperFocus prediction (bottom row) were matched with annotation results from Xenium (top row). For densely packed ROI #3 in **Fig. 2D**, SuperFocus was able to accurately delineate invasive tumor cells and distinguish them from immune and stromal cells. Myoepithelial cells, which usually show small, rounded, sac-like structures and were challenging to identify in the original Visium data, were clearly distinguished (ROI #4) by SuperFocus-predicted expression profiles. Furthermore, we evaluated the similarity in gene expression profiles across major cell types between SuperFocus predictions and Xenium measurements using heatmaps of average expressions of marker genes (**Fig. 2F**). The heatmaps demonstrated concordant marker gene expression patterns.

To validate the utility of our proposed quality control metrics, we assessed their ability to flag unreliable predictions using the ground-truth Xenium data. First, we evaluated the two feature-level diagnostic metrics: RSSE (Relative Sum-of-Squared-Errors) and ESL (Error Spatial Locality). When comparing these in-sample metrics against the true prediction error (measured against ground-truth Xenium profiles), we observed strong statistical concordance. Specifically, the RSSE significantly correlated with the ground-truth overall cell-level prediction error (**Fig. 2G** left; $r = 0.20$, P-value $= 0.002$), while the ESL closely tracked the ground-truth spatial locality of cell-level prediction residuals for each feature (**Fig. 2G** right; $r = 0.68$, P-value < 0.001). This confirms that these metrics, which were calculated solely from input spot data, the histological image, and the SuperFocus predictions at the finest resolution level, served as effective proxies for the true accuracy of the cell-level inferences for individual features. Next, we validated the per-cell prediction-credibility score, designed to flag potential hallucinations when predicting in regions without direct spot coverage. We computed this score for interstitial cells (those not overlapping Visium spots) and compared it to the true Pearson correlation between their SuperFocus predictions and matched Xenium measurements (**Fig. 2H**). The prediction-credibility score map exhibited high spatial concordance with the ground-truth accuracy map (MS-SSIM $= 0.729$, P-value < 0.001). This demonstrates that the credibility score reliably identified regions of lower credibility, effectively flagging potential overconfidence when extrapolating to the whole slide. In summary, both the feature-level diagnostics and the cell-level prediction-credibility score serve as effective metrics for objectively assessing the quality of SuperFocus predictions using only the training data.

Benchmarking on a VisiumHD human kidney dataset. We further benchmarked SuperFocus on a human kidney VisiumHD data (34) to enable validation with the same measurement technology on the same tissue section (**Fig. 3A**). The VisiumHD data was first binned to 64 μm spots (i.e., spots of size 64×64 μm^2), comparable to (albeit slightly larger than) the typical spot sizes in Visium and DBiT-seq experiments. We then trained SuperFocus on a sequence of 64, 32, 16 and 8 μm spots. The finest resolution level model was at the resolution of 8 μm where most spots contained at most one cell. For validation purpose, we further binned the VisiumHD data to 32, 16 and 8 μm spots, which served as the ground truth.

The predicted gene expressions at each resolution level by SuperFocus were compared to the binned VisiumHD data at the same resolution level to benchmark the multi-resolution performance of SuperFocus. We found that SuperFocus accurately predicted gene expressions across different resolutions (**Supplementary Fig. 2**). For instance, the transcript *NPHS2*, which provides instructions for making podocin and expressed exclusively in podocytes, solely enriched within the glomeruli of the kidney. In addition, the transcripts *SLC34A1* and *SLC4A1*, which are canonical markers for cells in the proximal tubule and distal part respectively, showed congruent spatial patterns between SuperFocus predictions and VisiumHD bins across resolutions. To further quantify the spatial similarity between SuperFocus prediction and ground truth, we adopted the same metric, MS-SSIM. At the finest resolution level (i.e., 8 μm spot), the MS-SSIM scores over a panel of 2010 spatially highly variable and kidney marker genes had a mean of 0.86 and a standard deviation of 0.12, demonstrating the high fidelity of SuperFocus prediction (**Fig. 3C**). To test the robustness of SuperFocus, we also trained SuperFocus with 50% and with 25% of the 64 μm spots. While the sizable decrease in sample size led to worse performance for 8 μm spot MS-SSIM scores as expected, the boxplots showed that the medians of MS-SSIM scores stayed above 0.6 (**Supplementary Fig. 3**).

The trained SuperFocus model at the finest resolution level was applied to the H&E image of the whole tissue section to conduct *in silico* prediction of gene expression profiles for each cell identified from the H&E image. To annotate cells with SuperFocus-predicted profiles for this dataset, we integrated them with a reference single-cell RNA-seq dataset (35) using Harmony (36). The reference dataset consisted of 107,701 cells in 15 major cell types from 31 healthy donors (**Fig. 3B1**). After Harmony integration, cells with SuperFocus-predicted expression profiles formed well-separated clusters which in turn aligned with major clusters in the reference data (**Fig. 3B2**), while non-perfect mixing was expected as scRNA-seq and VisiumHD are intrinsically different technologies. We annotated each cell with SuperFocus-predicted profile using majority voting by cell types of its k-nearest neighbors from the reference dataset after integration. With the annotation, we found that the heatmap of the average SuperFocus-predicted expression levels for marker genes of major kidney cell types showed distinct patterns (**Fig. 3D**). These patterns aligned well with known biology, with canonical marker genes predicted to

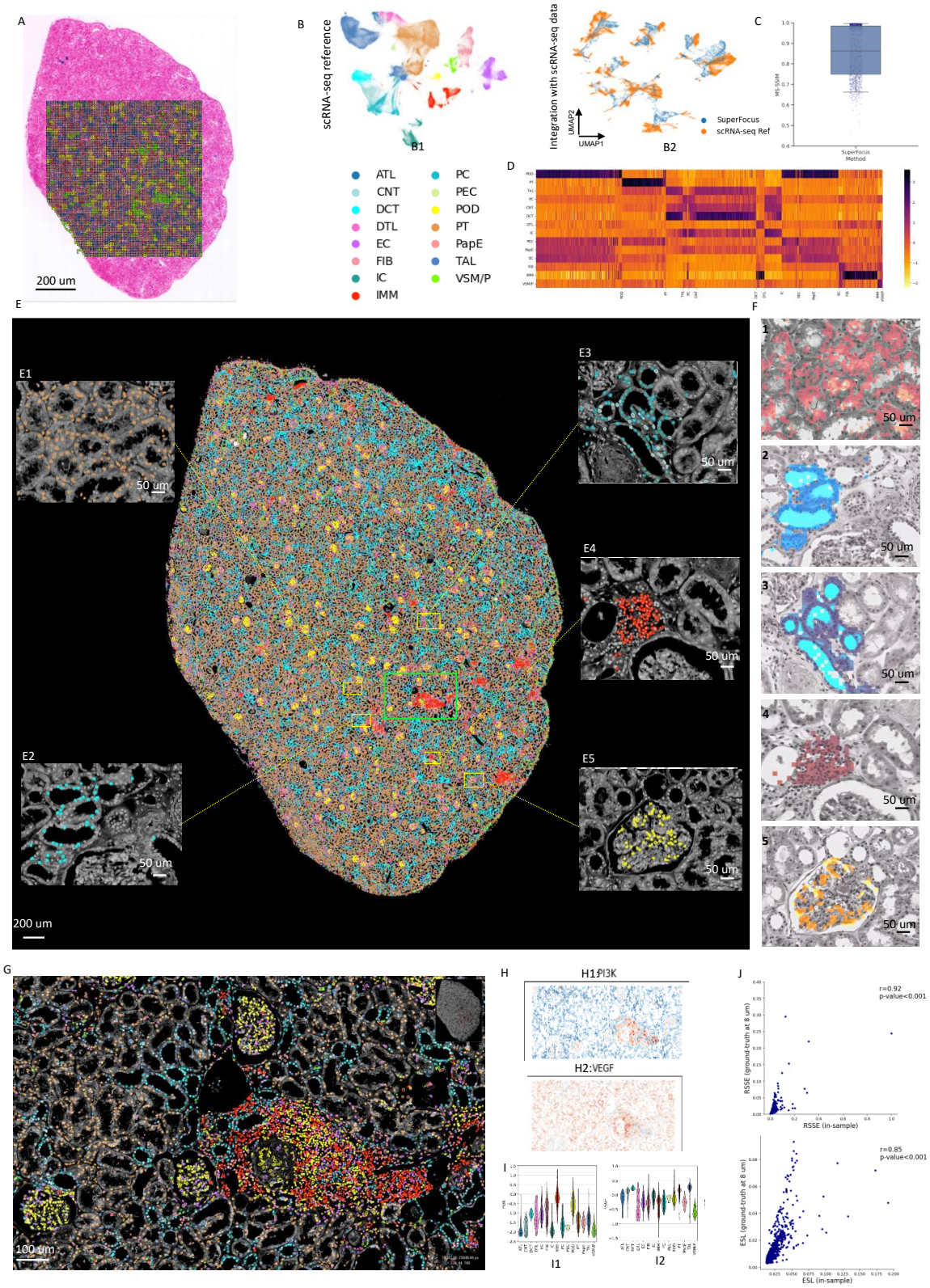

Figure 3: Benchmarking SuperFocus on a VisiumHD human kidney dataset. (A) High-resolution H&E image of human kidney sample with VisiumHD experiment region, spot size: $8\ \mu$m. **(B)** UMAP visualizations of scRNA-seq reference data from healthy human kidney samples (left) and of Harmony-integrated scRNA-seq reference data and SuperFocus-predicted cell-level gene expression profiles (right). **(C)** The boxplot of MS-SSIM scores quantifies similarities between SuperFocus-predicted expression levels and ground-truth VisiumHD measurements across 2010 spatially highly variable and kidney cell marker genes. **(D)** The heatmap of average SuperFocus-predicted gene expression profiles shows distinct patterns across cell types. **(E)** Gloabl and local spatial plots of annotated cell types of SuperFocus-predicted cell expression profiles. E1: proximal tubular cells, E2: Distal convoluted tubular cells, E3: Collecting duct cells, E4: Immune cells, E5: Podocytes. **(F)** F1 to F5 are corresponding regions to E1 to E5. The highlighted regions are distinct clusters from VisiumHD clustering results based on $8\ \mu$m data by 10X. **(G)** A zoomed-in view of the region highlighted in green in panel **E**. **(H)** Spatial plots of two pathway activity scores: PI3K (top) and VEGF (bottom). **(I)** PI3K (left) and VEGF (right) pathway activity scores across different cell types within the ROI in **G**. **(J)** Plots of in-sample diagnostic metrics RSSE (top) and ELS (bottom) computed from $64\ \mu$m spot training data show high correlations with ground-truth error metrics of overall prediction error and error spatial locality at $8\ \mu$m spot resolution level.

have high expressions in the corresponding cell types, e.g., *PODXL* in podocytes. These findings validated the ability of SuperFocus prediction to delineate cell types.

After mapping SuperFocus induced cell type annotations onto the tissue section, the spatial distribution of the cell types accurately reflected the kidney anatomical structure (**Fig. 3E**). For example, the apical surface of proximal tubule was covered with dense, long microvilli, forming a prominent brush border (**Fig. 3E1**), while the distal convoluted tubule (DCT) and the collecting duct system (PC, IC and CNT) had a smooth apical membrane (**Fig. 3E2 & E3**). In addition, immune cells resided between the tubules (**Fig. 3E4**), and podocytes were located within glomerulus (**Fig. 3E5**). These distinct spatial niches with cell-level resolution enabled by SuperFocus refinement of 64 μm spot-level data aligned nearly perfectly with distinct clusters of ground-truth VisiumHD 8 μm spots (**Fig. 3F**) provided by 10X (34).

We further zoomed in to a region enriched with immune cells (**Fig. 3E** ROI with green boundary & **Fig. 3G**). Unlike other glomeruli, SuperFocus prediction showed that the enlarged glomerulus in this region demonstrated inflammation and infiltration by immune cells, such as CD4+ T cells. This was supported by the higher activity score of the PI3K signaling pathway within this glomerulus (**Fig. 3H1**), which is a major regulator of cellular processes in podocytes, particularly when under stress and inflammation (37). The podocytes within this glomerulus showed elevated PI3K score (**Fig. 3I2**). In addition, we observed elevated activities through the hypoxia, the JAK-STAT and the MAPK signaling pathways (**Supplementary Fig. 3**). The glomerulus contains the most active and crucial VEGF signaling axis in human kidney, which is fundamental to maintaining the Glomerular Filtration Barrier. Furthermore, the VEGF pathway score derived from SuperFocus prediction showed elevated signaling within glomerulus (**Fig. 3H2**) and among podocytes (**Fig. 3I2**) in this region. Furthermore, we studied cell-cell communication with the SuperFocus-predicted cell expression profiles in this region using CellphoneDB (**Fig. 3J**). The analysis showed that immune cells interacted with various kidney cells, especially endothelial cells, principal cells, intercalated cells, and podocytes, via the CXCL12-ITGA4 axis, which governed the migration, homing, and retention of immune cells. We note that all the foregoing cell-level spatial analysis was conducted with SuperFocus-predicted profiles, and the findings were validated by ground-truth VisiumHD data (**Supplementary Fig. 3**).

Finally, we further validated the feature-level diagnostic metrics, RSSE and ESL, using the high-resolution VisiumHD dataset. Using only the 64 μm spot training data, RSSE and ESL remained strongly associated with their ground-truth counterparts computed by comparing SuperFocus predictions to VisiumHD measurements across 8 μm spots (**Fig. 3J**; RSSE (top): $r = 0.92$, P-value < 0.001; ESL (bottom): $r = 0.85$, P-value < 0.001). These correlations were substantially stronger than in the cross-platform Visium–Xenium benchmark (**Fig. 2G**), consistent with reduced technical variation between training and validation platforms.

SuperFocus unveils intratumoral cell-cell interactions in MALT lymphoma. We used SuperFocus to predict single-cell total RNA profiles on a MALT lymphoma (mucosa-associated lymphoid tissue lymphoma) within gastric mucosa H&E tissue section, with the SuperFocus model trained on an adjacent section with both H&E image (**Fig. 4A**) and Patho-DBiT measurements (**Fig. 4B**). SuperFocus-predicted RNA expressions aligned well with known pathological characteristics of the MALT lymphoma both within and outside of the region corresponding to the Patho-DBiT experiment FOV (**Supplementary Fig. 4**). For example, the transcript *MS4A1*, a marker for B cells, was enriched in the tumor regions, and the T cell marker *CD3D* concentrated around the periphery of follicles. The transcripts *XBP1* and *JCHAIN*, both of which are markers for plasma cells, were elevated in the lamina propria, where *MS4A1* expression level was low.

Next, we clustered the cells by applying a standard scRNA-seq data clustering pipeline on their SuperFocus-predicted expression profiles. Cell type annotation was then performed by taking into account both canonical gene markers and high-abundance transcripts within each cluster. See the upper panel in **Fig. 4C1** for the spatial plot of the annotated cell types from the SuperFocus-predicted expression profiles. Comparing the SuperFocus-enabled cell type annotations with the tissue architecture inferred from iStar (22, 38) (**Fig. 4C1**, lower panel), we found that SuperFocus enabled the spatial study of the sample at a much finer granularity, allowing truly single-cell resolution delineation of different spatial niches and tumor microenvironments. For example, malignant B cells from SuperFocus annotation aligned with the 9 iStar clusters (7, 11, 18, 17, 19, 22, 24, 25, 29) enriched with tumor B cells. The iStar cluster 25, annotated altogether as *INPP5D*+ B cells by iStar, consisted of 5 B cell subgroups and activated helper T cells (**Fig. 4C2 & D**). In cluster 25, a larger proportion of *FOXP3*+ B cells was identified. *FOXP3* has been found to suppress immune response (39) and agreed with the role of the *INPP5D* gene, which acts as a negative regulator of signaling in immune cells (40). The iStar cluster 29, characterized by enhanced B cells proliferation, exhibited an increased proportion of *TLR4*+ B cells compared to other regions of interest (ROIs) (**Fig. 4C3 & D**). The *TLR4* gene is known to promote B cell proliferation and survival via the ERK, the AKT and the NF-κB pathways (41). B cells with upregulated *EPB41* gene were present in the iStar cluster 13 (**Fig. 4C4 & D**). The *EPB41* gene plays a structural and regulatory role in connecting the membrane to the actin cytoskeleton in B cells (42), which aligned with the previous findings that B cells in this ROI underwent actin cytoskeleton organization (38) The upper right outer cortex was enriched with plasma cells (**Fig. 4C5 & D**), which was identified by both SuperFocus and iStar. Notably, SuperFocus further deciphered the complex cell type composition of these exemplifying ROIs and identified the presence of activated helper T cells in all of them. Previous studies discovered using customized immunochemistry panels and high-resolution imaging that the helper T cell population was more prevalent and highly active in MALT lymphoma compared to controls (43).

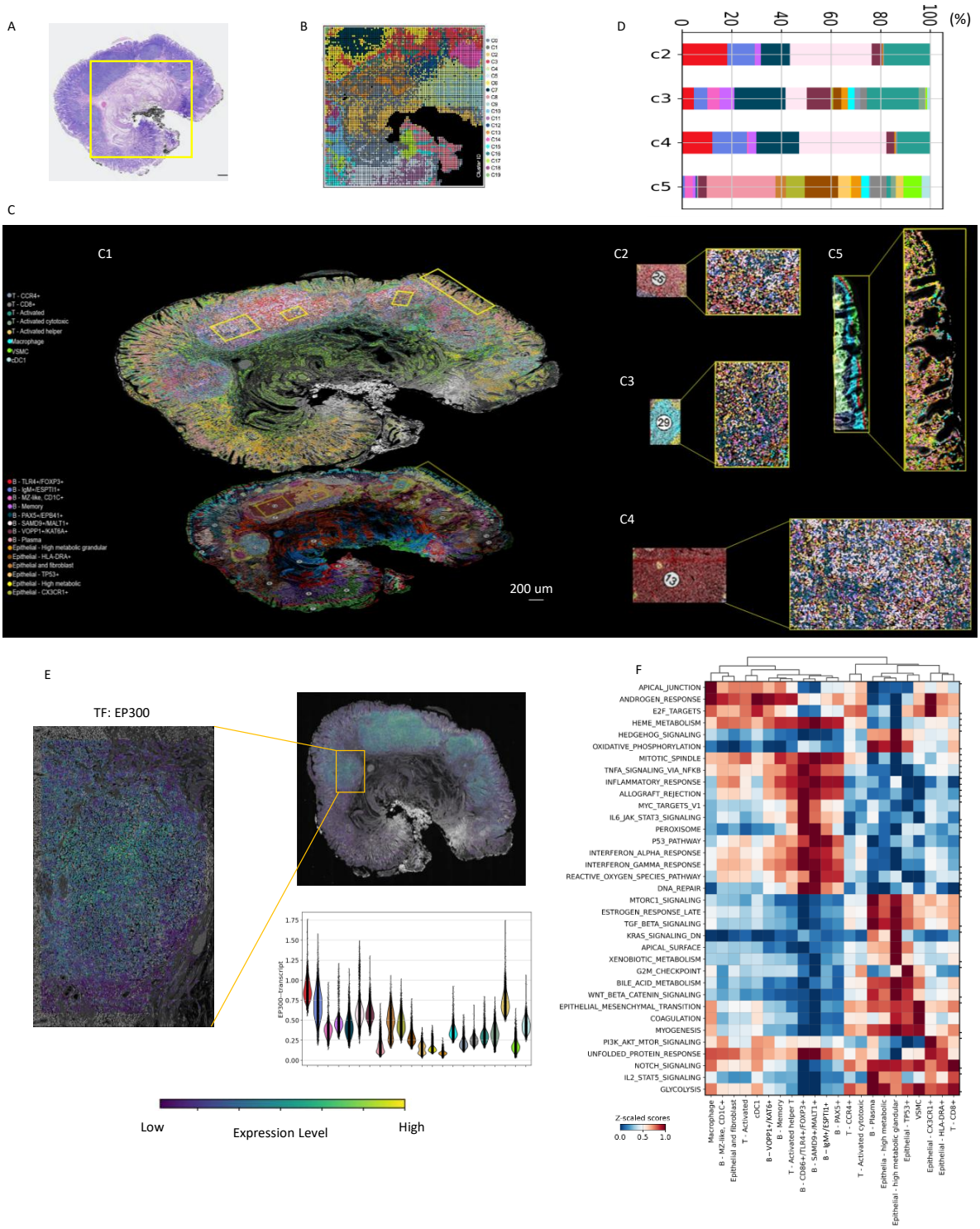

Figure 4: SuperFocus unveils intratumoral cell-cell interactions in MALT lymphoma. (A) High-resolution H&E image of MALT lymphoma sample with Patho-DBiT experiment region. **(B)** Spot-level Patho-DBiT data, spot size: $20\ \mu m$. **(C)** C1: Spatial plot of cells with annotation using SuperFocus-predicted cell-level gene expression profiles (top) with tissue architecture identified by iStar as reference (bottom, reproduced from (38) Figure 4E); C2-C5: SuperFocus deciphers cell types within niches identified by iStar. In the overall spatial plot and in each ROI, cells in the smaller view are colored by iStar niche annotation, and cells in the larger view are colored by SuperFocus cell type annotation. See legends to the left of C1 for the SuperFocus cell type annotation coloring scheme. **(D)** Decomposition of cell types within niches C2-C5 identified by iStar. See legends to the left of C1 for cell type coloring scheme. **(E)** Spatial plot of transcription factor EP300 in MALT lymphoma region (top), expression levels of *EP300* across different cell types within the region (bottom). **(F)** Hallmark pathway analysis results based on SuperFocus-predicted single-cell gene expression profiles.

These helper T cells play a promoting role in MALT lymphoma by creating a supportive microenvironment that enables malignant B cells to better survive and proliferate (44). SuperFocus was able to gain comparable insights at single-cell spatial resolution from spot-level data without a targeted panel, providing single-cell level details of iStar-annotated spatial niches beyond a single enriched cell type.

Furthermore, we analyzed cell-cell communications between different cell types in this MALT lymphoma sample using the SuperFocus-predicted single cell gene expression profiles (**Fig. 4E**). The cell type annotation from SuperFocus identified MZ-like and memory B cells, macrophages and cDC1 cells located in the periphery of follicles, other B cell subgroups except plasma cells along with activated helper T cells mainly in the central tumor regions, and the lamina propria consisting of different types of epithelial cells, plasma cells, smooth muscle cells and some T cells. The Hallmark pathway analysis revealed that cells in the periphery of follicles, the central tumoral regions, and the lamina propria interacted via different pathways (**Fig. 4C1**). For example, the NF-κB and the JAK-STAT3 pathways, two of the most critical pathways in MALT lymphoma, were active in cells, especially *TLR4*+ B cells, located in the central tumor regions (45). Furthermore, malignant B cells showed enhanced IFN-α and IFN-γ pathway activities , which are critical in the pathogenesis and progression of MALT lymphoma, particularly those associated with chronic infection (46). Additionally, mitotic spindle assembly, that directly links to the uncontrolled proliferation of malignant B cells, was found to be active in tumor regions. Meanwhile, some pathways exhibited inconsistent activity scores in different tumor regions within this sample (**Supplementary Fig. 5**). These results not only illustrated tumor heterogeneity but also demonstrated the ability of SuperFocus to faithfully capture important biological signals in its prediction.

Finally, TF scoring results obtained from SuperFocus prediction identified TFs that were more active in the MALT tumors (**Supplementary Fig. 6**). In particular, this sample showed upregulated EP300 expression (**Fig. 4D, Supplementary Fig. 6**). The EP300 transcription factor is a key player in the pathogenesis of B-cell lymphomas through its function as a major histone acetyltransferase (HAT) and transcriptional co-activator (47). Besides, NOTCH1, one of the known aberrant activators often linked to the pathogenesis of B-cell malignancies (48), was also predicted to have increased expression levels within the tumor regions (**Supplementary Fig. 6**). Additionally, SuperFocus enabled the examination of TF expression levels within each cell, identifying *TLR4*+, *IgM*+ and *ESPTI1*+ B cells and activated T helper cells in the central tumor regions with aberrant increase in both TFs, and warranted further investigation into how activated TFs mediated cells within tumor regions.

SuperFocus infers single-cell peak matrix from spot-level spatial ATAC-seq data and enables spatial gene regulatory network analysis. We evaluated SuperFocus on a human hippocampus co-mapping data, where both spot-level spatial ATAC-seq and mRNA-seq measurements were available (25) (**Fig. 5A2**). We first trained SuperFocus on the spatial ATAC-seq modality and the H&E image of an immediately adjacent section (**Fig. 5A1**). The sections were aligned by STalign (32) with anchor points. Then we used the trained model to predict single-cell peak vectors across all cells on the H&E image.

Next, we conducted unsupervised clustering of the SuperFocus-predicted single-cell peak vectors and annotated each cluster based on the peak-inferred gene activity scores (49) of marker gene (**Fig. 5C**). For instance, open chromatin profiles at the coding regions of *OLIG2 and MOG* gene identified oligodendrocytes, while *RBFOX3* identified neurons. Immunohistochemistry (IHC) for key cell type–specific marker proteins was performed on adjacent sections by spatial proteomics (Akoya Phenocycler, 25-plex) and used as ground truth for cell type annotation. A board-certified neuropathologist confirmed the identification of major cell types in IHC results, including neurons, oligodendrocytes, astrocytes, microglia, vascular cells, leptomeningeal cells, and choroid plexus cells, within tissue section (**Fig. 5A3**).

Comparing **Fig. 5A3** and **Fig. 5C**, we found SuperFocus and IHC cell type annotations were highly aligned, both in turn aligned well with the anatomical structure of human hippocampus. SuperFocus-predicted peak profiles enabled us to accurately locate neurons in Dentate Gyrus (DG Neuron) and Cornu Ammonis (CA Neuron), oligodendrocytes (Olig), and astrocytes (Astro). Dentate gyrus neurons were densely packed within the granule cell layer, whereas astrocytes and oligodendrocytes were distributed across the molecular and polymorphic layers of the Dentate Gyrus. The fimbria was enriched with oligodendrocytes and largely devoid of neurons. Moreover, SuperFocus-predicted peak profiles successfully discriminated between Choroid Plexus (ChPx), Vascular (Vas) and Leptomeningeal (LM) cells. To further validate the biological faithfulness of SuperFocus-predicted single-cell epigenomic information, we examined the spatial distribution of SuperFocus-predicted mRNA expression levels of key marker genes by further applying SuperFocus on the mRNA-seq modality of this co-profiled spatial dataset. We found that the *PROX1* gene, a marker for mature granule neurons, was highly expressed in Dentate Gyrus granule cell layer (**Fig. 5B**). Moreover, *MOG* was enriched in Oligodendrocytes, *SST* was expressed where neurons were identified, regions with high expressions of *SLC1A2* agreed with the locations of Astrocytes, and *PECAM1* showed elevated expression level in Vascular cells (**Supplementary Fig. 7**). The pseudo-coverage plot of SuperFocus-predicted peaks showed that the genome was more accessible within the *PROX1* gene region for Dentate Gyrus granule neurons than other cell types (**Fig. 5D, Supplementary Fig. 7**).

Furthermore, the SuperFocus-predicted single-cell open chromatin peak profiles offers a new perspective to investigate TF binding activity across individual cells with spatial contexts in an intact tissue. We calculated the TF deviation score (50) to evaluate the level of accessibility at genomic regions, which contain a specific TF's binding motif, deviated from the background. The highly variable TF motifs for

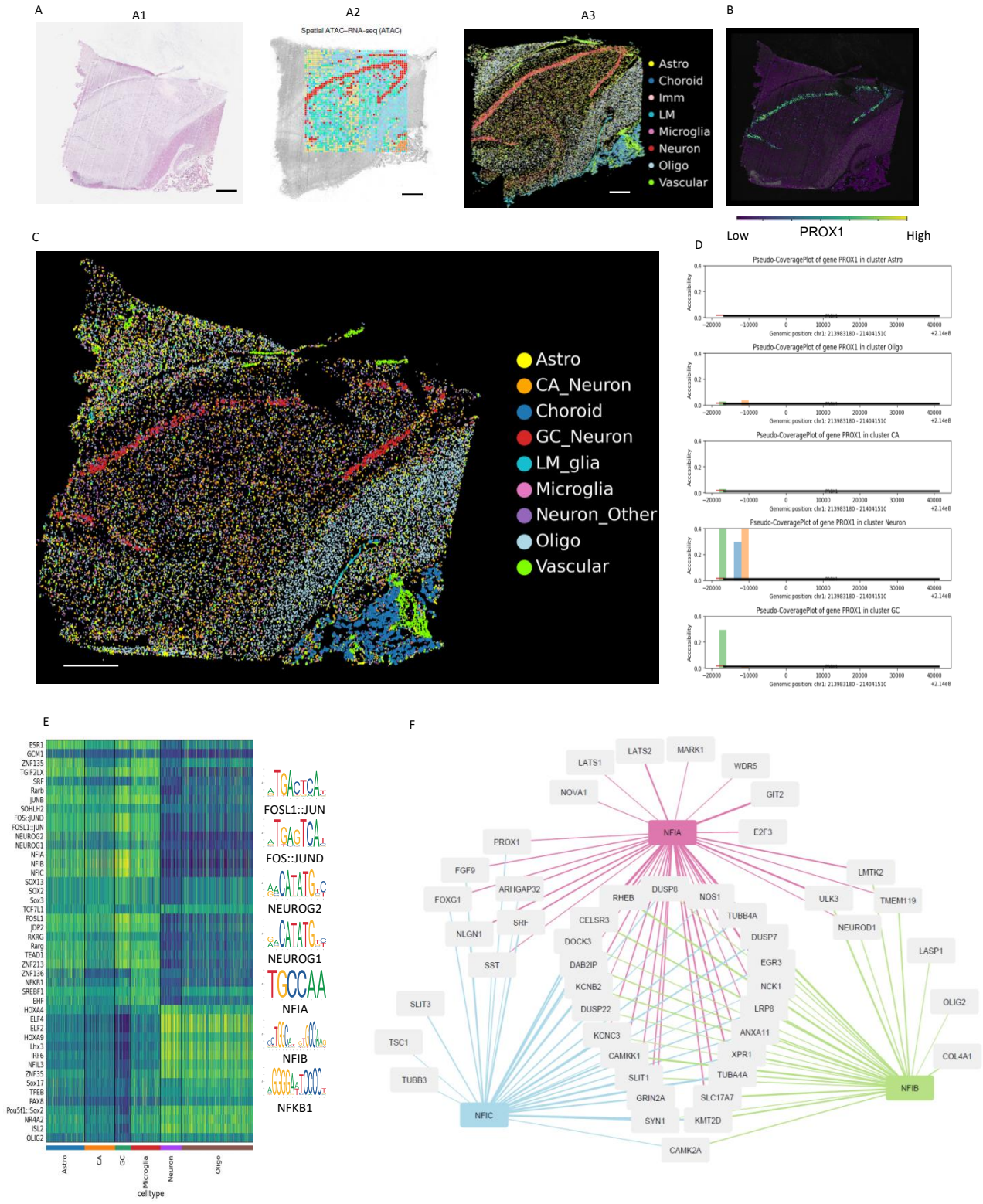

Figure 5: Application of SuperFocus on a spot-level spatial ATAC-seq human hippocampus dataset. (A) A1: High-resolution H&E image of the human hippocampus sample; A2: Spot-level Spatial ATAC-RNA-seq data for human hippocampus sample (only ATAC results shown here), spot size: $50\ \mu$m; A3: Spatial plot of cells annotated from single-cell 25-plex IHC data on an adjacent section. **(B)** Spatial plot of SuperFocus-predicted single-cell level *PROX1* gene expression; **(C)** Cell type annotation based on SuperFocus-predicted single-cell level peak profiles; **(D)** Pseudo-coverage plots of the gene *PROX1* region across different cell types inferred from SuperFocus-predicted cell-level peak profiles; **(E)** Heatmap of TF deviation scores inferred from SuperFocus-predicted cell-level peak profiles across different cell types; **(F)** A gene regulatory network related to three TFs, NFIA, NFIB and NFIC, based on SuperFocus-predicted cell-level gene expression and peak profiles. Scale bars: 1mm.

each cell type were then identified, and the heatmap of the standardized TF deviation scores was plotted (**Fig. 5E**). Neurons in the Dentate Gyrus and Cornu Ammonis showed sizably higher accessibility in the genomic regions containing the motifs of the FOSL1::JUN, FOS::JUN, NEUROG1 and NEUROG2 TFs. The genomes of homeostatic microglia, activated microglia, and other resident immune cells of the central nervous system exhibited greater accessibility around the NFKB1 TF motif region, indicating higher activity via the NF-κB pathway.

Discussion

Spot-based spatial omics paired with histology offers one of the most scalable compromises in the cost–resolution–scope trilemma of spatial data acquisition. However, spot-level measurements blur cell-level variation and typically provide only a limited profiled field of view. Motivated by the need to recover whole-slide, single-cell–resolved molecular landscapes from these standard inputs without increasing experimental burden, we developed SuperFocus, which enables high-fidelity, whole-slide, cell-level prediction of high-dimensional omics features from spot-based measurements and provides two per-feature in-sample diagnostic metrics and a per-cell prediction-credibility score to flag potentially unreliable predictions. SuperFocus enables single-cell–resolved inference by defining a multiscale sequence of prediction grids and transferring information from coarse spot measurements to progressively finer resolutions via a constrained cascading imputation procedure. This procedure enforces consistency with observed spot-level signals while mitigating hallucination.

In this work, we demonstrated SuperFocus on spot-based spatial transcriptomics and spatial ATAC-seq. Although not exhaustively evaluated beyond these settings, its modality-agnostic design provides a clear path toward extending the framework to additional spot-based spatial omics modalities, contingent on appropriate modality-specific validation.

SuperFocus implicitly assumes that the spot-level experiment is performed on region(s) of interest (ROIs) whose histological and cellular composition is representative of the broader whole-slide tissue on which single-cell molecular details are being reconstructed. When the assayed ROI undersamples rare morphologies, spatially localized programs, or transitional states, whole-slide prediction becomes extrapolative. Therefore, even when within-ROI fidelity is strong, inferred profiles for cells in underrepresented spatial contexts may be biased and more prone to artifacts. While the proposed prediction-credibility score can flag such cells *post hoc*, it is more cost effective to prevent this from happening by profiling an appropriate ROI in the first place. ROI selection is therefore an important upstream problem. Visual–omics and digital pathology foundation models (16–20, 51–54) can help formalize ROI selection by quantifying histologic heterogeneity from H&E and prioritizing ROIs that maximize histologic heterogeneity coverage (55) or molecular information content.

Beyond single-slide applications, the SuperFocus paradigm could extend to serial sections and 3D reconstruction by integrating inferred cell-level profiles across slices. This multi-section extension faces a major additional hurdle: robust cross-section harmonization of both spot-level measurements and histological images. Existing multi-slice alignment/stitching methods for spot-level spatial omics (32, 56, 57) provide useful foundations, but principled batch correction for spatial transcriptomics and other spatial modalities will be essential for reliable 3D cell-level inference from serial sections with spot-based measurements.

DATA AVAILABILITY

This study did not generate any new experimental data.
The human breast Cancer dataset by Xenium & Visium was from: https://www.10xgenomics.com/products/xenium-in-situ/preview-dataset-human-breast.
The human healthy kidney dataset by VisiumHD was from https://www.10xgenomics.com/datasets/visium-hd-cytassist-gene-expression-libraries-human-kidney-ffpe-v4.
The human MALT lymphoma dataset by Patho-DBiT was from GSE274641.
The human hippocampus dataset by Spatial ATAC–RNA-seq was from GSE205055.

CODE AVAILABILITY

The SuperFocus Python package can be found in the GitHub repository: `https://github.com/yaolu53/SuperFocus`.

ACKNOWLEDGEMENTS

Computational data analysis was conducted with Yale High Performance Computing clusters (HPC). We acknowledge the support received from the U.S. National Institutes of Health including grants U54CA274509, U54CA268083, UH3CA257393, RF1MH128876, U54AG079759, U54AG076043, R01CA245313, RM1MH132648 (all to R.F.), and U01CA294514 (to R.F., M.X., and Z.M.), and from the U.S. National Science Foundation in grant DMS-2245575 (to Z.M.). Cartoons in Figures 1 were created with BioRender.com.
This article reflects the views of the authors and should not be construed as representing the views or policies of the institutions that provided funding.

AUTHOR CONTRIBUTIONS

Conceptualization: Y.L., R.F., Z.M.
Algorithm Development and Implementation: Y.L., Z.M.
Analysis: Y.L., M.X., Y.X., R.F., Z.M.
Contribution of Material and Expertise: A.E., S.B., Z.B., M.X., Y.X., R.F., Z.M.
Supervision: M.X, Y.X., R.F., Z.M.

CONFLICT OF INTERESTS

R.F. is scientific founder and adviser for IsoPlexis, Singleron Biotechnologies, and AtlasXomics. The interests of R.F. were reviewed and managed by Yale University Provost's Office in accordance with the University's conflict of interest policies. M.X. has served as consultant for Treeline Biosciences, Pure Marrow, and Seattle Genetics. The remaining authors declare no competing interests.

Reference

1. Emma Lundberg and Georg HH Borner. Spatial proteomics: a powerful discovery tool for cell biology. *Nature Reviews Molecular Cell Biology*, 20(5):285–302, 2019.
2. Method of the year 2020: spatially resolved transcriptomics. *Nature methods*, 18(1):9–14, 2021.
3. Sabrina M Lewis, Marie-Liesse Asselin-Labat, Quan Nguyen, Jean Berthelet, Xiao Tan, Verena C Wimmer, Delphine Merino, Kelly L Rogers, and Shalin H Naik. Spatial omics and multiplexed imaging to explore cancer biology. *Nature methods*, 18(9):997–1012, 2021.
4. Anjali Rao, Dalia Barkley, Gustavo S França, and Itai Yanai. Exploring tissue architecture using spatial transcriptomics. *Nature*, 596(7871):211–220, 2021.
5. Dario Bressan, Giorgia Battistoni, and Gregory J Hannon. The dawn of spatial omics. *Science*, 381(6657):eabq4964, 2023.
6. Logan A Walsh and Daniela F Quail. Decoding the tumor microenvironment with spatial technologies. *Nature immunology*, 24(12):1982–1993, 2023.
7. Method of the year 2024: spatial proteomics. *Nat Methods*, 21:2195–2196, 2024.
8. Lambda Moses and Lior Pachter. Museum of spatial transcriptomics. *Nature methods*, 19 (5):534–546, 2022.
9. Julienne L Carstens, Santhoshi N Krishnan, Arvind Rao, Anna G Sorace, Erin H Seeley, Sammy Ferri-Borgogno, and Jared K Burks. Spatial multiplexing and omics. *Nature Reviews Methods Primers*, 4(1):54, 2024.
10. Patrik L Ståhl, Fredrik Salmén, Sanja Vickovic, Anna Lundmark, José Fernández Navarro, Jens Magnusson, Stefania Giacomello, Michaela Asp, Jakub O Westholm, Mikael Huss, et al. Visualization and analysis of gene expression in tissue sections by spatial transcriptomics. *Science*, 353(6294):78–82, 2016.
11. Yang Liu, Mingyu Yang, Yanxiang Deng, Graham Su, Archibald Enninful, Cindy C Guo, Toma Tebaldi, Di Zhang, Dongjoo Kim, Zhiliang Bai, et al. High-spatial-resolution multi-omics sequencing via deterministic barcoding in tissue. *Cell*, 183(6):1665–1681, 2020.

12. Yanxiang Deng, Marek Bartosovic, Sai Ma, Di Zhang, Petra Kukanja, Yang Xiao, Graham Su, Yang Liu, Xiaoyu Qin, Gorazd B Rosoklija, et al. Spatial profiling of chromatin accessibility in mouse and human tissues. *Nature*, 609(7926):375–383, 2022.
13. Richard J Chen, Chengkuan Chen, Yicong Li, Tiffany Y Chen, Andrew D Trister, Rahul G Krishnan, and Faisal Mahmood. Scaling vision transformers to gigapixel images via hierarchical self-supervised learning. In *Proceedings of the IEEE/CVF conference on computer vision and pattern recognition*, pages 16144–16155, 2022.
14. Xiyue Wang, Sen Yang, Jun Zhang, Minghui Wang, Jing Zhang, Wei Yang, Junzhou Huang, and Xiao Han. Transformer-based unsupervised contrastive learning for histopathological image classification. *Medical image analysis*, 81:102559, 2022.
15. Xiyue Wang, Yuexi Du, Sen Yang, Jun Zhang, Minghui Wang, Jing Zhang, Wei Yang, Junzhou Huang, and Xiao Han. Retccl: Clustering-guided contrastive learning for whole-slide image retrieval. *Medical image analysis*, 83:102645, 2023.
16. Zhi Huang, Federico Bianchi, Mert Yuksekgonul, Thomas J Montine, and James Zou. A visual–language foundation model for pathology image analysis using medical twitter. *Nature medicine*, 29(9):2307–2316, 2023.
17. Richard J Chen, Tong Ding, Ming Y Lu, Drew FK Williamson, Guillaume Jaume, Andrew H Song, Bowen Chen, Andrew Zhang, Daniel Shao, Muhammad Shaban, et al. Towards a general-purpose foundation model for computational pathology. *Nature medicine*, 30(3): 850–862, 2024.
18. Ming Y Lu, Bowen Chen, Drew FK Williamson, Richard J Chen, Ivy Liang, Tong Ding, Guillaume Jaume, Igor Odintsov, Long Phi Le, Georg Gerber, et al. A visual-language foundation model for computational pathology. *Nature medicine*, 30(3):863–874, 2024.
19. Hanwen Xu, Naoto Usuyama, Jaspreet Bagga, Sheng Zhang, Rajesh Rao, Tristan Naumann, Cliff Wong, Zelalem Gero, Javier González, Yu Gu, et al. A whole-slide foundation model for digital pathology from real-world data. *Nature*, 630(8015):181–188, 2024.
20. Eugene Vorontsov, Alican Bozkurt, Adam Casson, George Shaikovski, Michal Zelechowski, Kristen Severson, Eric Zimmermann, James Hall, Neil Tenenholtz, Nicolo Fusi, et al. A foundation model for clinical-grade computational pathology and rare cancers detection. *Nature medicine*, 30(10):2924–2935, 2024.
21. Ludvig Bergenstråhle, Bryan He, Joseph Bergenstråhle, Xesús Abalo, Reza Mirzazadeh, Kim Thrane, Andrew L Ji, Alma Andersson, Ludvig Larsson, Nathalie Stakenborg, et al. Super-resolved spatial transcriptomics by deep data fusion. *Nature biotechnology*, 40(4): 476–479, 2022.
22. Daiwei Zhang, Amelia Schroeder, Hanying Yan, Haochen Yang, Jian Hu, Michelle Y. Y. Lee, Kyung S. Cho, Katalin Susztak, George X. Xu, Michael D. Feldman, Edward B. Lee, Emma E. Furth, Linghua Wang, and Mingyao Li. Inferring super-resolution tissue architecture by integrating spatial transcriptomics with histology. *Nature Biotechnology*, 42(9): 1372–1377, 2024. ISSN 1087-0156 1546-1696. doi: 10.1038/s41587-023-02019-9.
23. Pengzhi Zhang, Weiqing Chen, Tu N Tran, Minghao Zhou, Kaylee N Carter, Ibrahem Kandel, Shengyu Li, Xen Ping Hoi, Yuxing Sun, Li Lai, et al. Thor: a platform for cell-level investigation of spatial transcriptomics and histology. *Nature Communications*, 16(1):7178, 2025.
24. Zhiliang Bai, Dingyao Zhang, Yan Gao, Bo Tao, Daiwei Zhang, Shuozhen Bao, Archibald Enninful, Yadong Wang, Haikuo Li, Graham Su, et al. Spatially exploring rna biology in archival formalin-fixed paraffin-embedded tissues. *Cell*, 187(23):6760–6779, 2024.
25. Di Zhang, Yanxiang Deng, Petra Kukanja, Eneritz Agirre, Marek Bartosovic, Mingze Dong, Cong Ma, Sai Ma, Graham Su, Shuozhen Bao, et al. Spatial epigenome–transcriptome co-profiling of mammalian tissues. *Nature*, 616(7955):113–122, 2023.
26. Fabian Hörst, Moritz Rempe, Lukas Heine, Constantin Seibold, Julius Keyl, Giulia Baldini, Selma Ugurel, Jens Siveke, Barbara Grünwald, Jan Egger, et al. Cellvit: Vision transformers for precise cell segmentation and classification. *Medical Image Analysis*, 94:103143, 2024.
27. Sinno Jialin Pan and Qiang Yang. A survey on transfer learning. *IEEE Transactions on knowledge and data engineering*, 22(10):1345–1359, 2009.
28. Archibald Enninful, Zhaojun Zhang, Dmytro Klymyshyn, Hailing Zong, Zhiliang Bai, Negin Farzad, Graham Su, Alev Baysoy, Jungmin Nam, Mingyu Yang, et al. Integration of imaging-based and sequencing-based spatial omics mapping on the same tissue section via dbitplus. *bioRxiv*, 2024.
29. Zhi-Jie Cao and Ge Gao. Multi-omics single-cell data integration and regulatory inference with graph-linked embedding. *Nature Biotechnology*, 40(10):1458–1466, 2022.
30. Shuxiao Chen, Bokai Zhu, Sijia Huang, John W Hickey, Kevin Z Lin, Michael Snyder, William J Greenleaf, Garry P Nolan, Nancy R Zhang, and Zongming Ma. Integration of spatial and single-cell data across modalities with weakly linked features. *Nature Biotechnology*, 42(7):1096–1106, 2024.
31. Amanda Janesick, Robert Shelansky, Andrew D Gottscho, Florian Wagner, Stephen R Williams, Morgane Rouault, Ghezal Beliakoff, Carolyn A Morrison, Michelli F Oliveira, Jordan T Sicherman, et al. High resolution mapping of the tumor microenvironment using integrated single-cell, spatial and in situ analysis. *Nature communications*, 14(1):8353, 2023.
32. Kalen Clifton, Manjari Anant, Gohta Aihara, Lyla Atta, Osagie K. Aimiuwu, Justus M. Kebschull, Michael I. Miller, Daniel Tward, and Jean Fan. Stalign: Alignment of spatial transcriptomics data using diffeomorphic metric mapping. *Nature Communications*, 14(1):8123, 2023. doi: 10.1038/s41467-023-43915-7.
33. Zhou Wang, Eero P Simoncelli, and Alan C Bovik. Multiscale structural similarity for image quality assessment. In *The thrity-seventh asilomar conference on signals, systems & computers, 2003*, volume 2, pages 1398–1402. Ieee, 2003.
34. 10x Genomics. Visium HD Spatial Gene Expression Library, Human Kidney (FFPE). 10x Genomics Datasets, March 2025. Published Mar 6, 2025.
35. Blue B. Lake, Rajasree Menon, Seth Winfree, Qiwen Hu, Ricardo Melo Ferreira, Kian Kalhor, Daria Barwinska, Edgar A. Otto, Michael Ferkowicz, Dinh Diep, Nongluk Plongthongkum, Amanda Knoten, Sarah Urata, Laura H. Mariani, Abhijit S. Naik, Sean Eddy, Bo Zhang, Yan Wu, Diane Salamon, James C. Williams, Xin Wang, Karol S. Balderrama, Paul J. Hoover, Evan Murray, Jamie L. Marshall, Teia Noel, Anitha Vijayan, Austin Hartman, Fei Chen, Sushrut S. Waikar, Sylvia E. Rosas, Francis P. Wilson, Paul M. Palevsky, Krzysztof Kiryluk, John R. Sedor, Robert D. Toto, Chirag R. Parikh, Eric H. Kim, Rahul Satija, Anna Greka, Evan Z. Macosko, Peter V. Kharchenko, Joseph P. Gaut, Jeffrey B. Hodgin, Richard Knight, Stewart H. Lecker, Isaac Stillman, Afolarin A. Amodu, Titlayo Ilori, Shana Maikhor, Insa Schmidt, Gearoid M. McMahon, Astrid Weins, Nir Hacohen, Lakeshia Bush, Agustin Gonzalez-Vicente, Jonathan Taliercio, John O'toole, Emilio Poggio, Leslie Cooperman, Stacey Jolly, Leal Herlitz, Jane Nguyen, Ellen Palmer, Dianna Sendrey, Kassandra Spates-Harden, Paul Appelbaum, Jonathan M. Barasch, Andrew S. Bomback, Vivette D. D'Agati, Karla Mehl, Pietro A. Canetta, Ning Shang, Olivia Balderes, Satoru Kudose, Laura Barisoni, Theodore Alexandrov, Yinghua Cheng, Kenneth W. Dunn, Katherine J. Kelly, Timothy A. Sutton, Yumeng Wen, Celia P. Corona-Villalobos, Steven Menez, Avi Rosenberg, Mohammed Atta, Camille Johansen, Jennifer Sun, Neil Roy, Mark Williams, Evren U. Azeloglu, Cijang He, Ravi Iyengar, Jens Hansen, Yuguang Xiong, Brad Rovin, Samir Parikh, Sethu M. Madhavan, Christopher R. Anderton, Ljiljana Pasa-Tolic, et al. An atlas of healthy and injured cell states and niches in the human kidney. *Nature*, 619(7970):585–594, 2023. ISSN 0028-0836 1476-4687. doi: 10.1038/s41586-023-05769-3.
36. Ilya Korsunsky, Nghia Millard, Jean Fan, Kamil Slowikowski, Fan Zhang, Kevin Wei, Yuriy Baglaenko, Michael Brenner, Po-ru Loh, and Soumya Raychaudhuri. Fast, sensitive and accurate integration of single-cell data with harmony. *Nature methods*, 16(12):1289–1296, 2019.
37. Federica Barutta, Stefania Bellini, and Gabriella Gruden. Mechanisms of podocyte injury and implications for diabetic nephropathy. *Clinical Science*, 136(7):493–520, 2022.
38. Zhiliang Bai, Dingyao Zhang, Yan Gao, Bo Tao, Daiwei Zhang, Shuozhen Bao, Archibald Enninful, Yadong Wang, Haikuo Li, Graham Su, Xiaolong Tian, Ningning Zhang, Yang Xiao, Yang Liu, Mark Gerstein, Mingyao Li, Yi Xing, Jun Lu, Mina L. Xu, and Rong Fan. Spatially exploring rna biology in archival formalin-fixed paraffin-embedded tissues. *Cell*, 187(23): 6760–6779.e24, 2024. ISSN 00928674. doi: 10.1016/j.cell.2024.09.001.
39. Endeshaw Chekol Abebe, Tadesse Asmamaw Dejenie, Teklie Mengie Ayele, Nega Dagnew Baye, Assefa Agegnehu Teshome, and Zelalem Tilahun Muche. The role of regulatory b cells in health and diseases: A systemic review. *Journal of Inflammation Research*, Volume 14:75–84, 2021. ISSN 1178-7031. doi: 10.2147/jir.S286426.
40. National Center for Biotechnology Information. Gene: INSL3 – insulin like 3 [Homo sapiens (human)]. https://www.ncbi.nlm.nih.gov/gene/3635, 2025. Gene ID: 3635, Accessed: 2025-12-24.
41. Edina Schweighoffer, Josquin Nys, Lesley Vanes, Nicholas Smithers, and Victor L. J. Tybulewicz. Tlr4 signals in b lymphocytes are transduced via the b cell antigen receptor and syk. *Journal of Experimental Medicine*, 214(5):1269–1280, 2017. ISSN 0022-1007 1540-9538. doi: 10.1084/jem.20161117.
42. Marcela Salomao, Xihui Zhang, Yang Yang, Soohee Lee, John H. Hartwig, Joel Anne Chasis, Narla Mohandas, and Xiuli An. Protein 4.1r-dependent multiprotein complex: New insights into the structural organization of the red blood cell membrane. *Proceedings of the National Academy of Sciences*, 105(23):8026–8031, 2008. ISSN 0027-8424 1091-6490. doi: 10.1073/pnas.0803225105.
43. Roberto Tamma, Giuseppe Ingravallo, Tiziana Annese, Michela De Giorgis, Fabrizia Di Giovanni, Francesco Gaudio, Tommasina Perrone, Pellegrino Musto, Giorgina Specchia, and Domenico Ribatti. Tumor cell microenvironment and microvessel density analysis in malt type lymphoma. *Anticancer Research*, 41(3):1291–1297, 2021. ISSN 0250-7005 1791-7530. doi: 10.21873/anticanres.14886.
44. M. Guindi. Role of activated host t cells in the promotion of malt lymphoma growth. *Seminars in Cancer Biology*, 10(5):341–344, 2000. ISSN 1044579X. doi: 10.1006/scbi.2000.0351.
45. Barbara Uhl, Katharina T. Prochazka, Karoline Fechter, Katrin Pansy, Hildegard T. Greinix, Peter Neumeister, and Alexander J. A. Deutsch. Impact of the microenvironment on the pathogenesis of mucosa-associated lymphoid tissue lymphomas. *World Journal of Gastrointestinal Oncology*, 14(1):153–162, 2022. ISSN 1948-5204. doi: 10.4251/wjgo.v14.i1.153.
46. Koji Yamamoto, Yasuyuki Kondo, Shunsuke Ohnishi, Masaru Yoshida, Toshiro Sugiyama, and Naoya Sakamoto. The tlr4–trif–type 1 ifn–ifn-γ pathway is crucial for gastric malt lymphoma formation after helicobacter suis infection. *iScience*, 24(9), 2021. ISSN 25890042. doi: 10.1016/j.isci.2021.103064.
47. Yu Zhu, Zi Wang, Yanan Li, Hongling Peng, Jing Liu, Ji Zhang, and Xiaojuan Xiao. The role of crebbp/ep300 and its therapeutic implications in hematological malignancies. *Cancers*, 15(4), 2023. ISSN 2072-6694. doi: 10.3390/cancers15041219.
48. Patricia Johansson, Ludger Klein-Hitpass, Florian Grabellus, Georg Arnold, Wolfram Klapper, Roman Pförtner, Ulrich Dührsen, Anja Eckstein, Jan Dürig, and Ralf Küppers. Recurrent mutations in nf-κb pathway components, kmt2d, and notch1/2 in ocular adnexal malt-type marginal zone lymphomas. *Oncotarget*, 7(38):62627–62639, 2016. ISSN 1949-2553. doi: 10.18632/oncotarget.11548.
49. Tim Stuart, Andrew Butler, Paul Hoffman, Christoph Hafemeister, Efthymia Papalexi, William M Mauck, Yuhan Hao, Marlon Stoeckius, Peter Smibert, and Rahul Satija. Comprehensive integration of single-cell data. *Cell*, 177(7):1888–1902, 2019.
50. Alicia N Schep, Buenrostro Wu, Jason D Buenrostro, and William J Greenleaf. chromVAR: inferring transcription-factor-associated chromatin accessibility from single-cell epigenomic data. *Nature Methods*, 14(10):975–978, 2017.
51. Shengyi Hua, Fang Yan, Tianle Shen, Lei Ma, and Xiaofan Zhang. Pathoduet: Foundation models for pathological slide analysis of h&e and ihc stains. *Medical Image Analysis*, 97: 103289, 2024.
52. Weiqing Chen, Pengzhi Zhang, Tu N Tran, Yiwei Xiao, Shengyu Li, Vrutant V Shah, Hao Cheng, Kristopher W Brannan, Keith Youker, Li Lai, et al. A visual–omics foundation model to bridge histopathology with spatial transcriptomics. *Nature Methods*, pages 1–15, 2025.
53. Tinglin Huang, Tianyu Liu, Mehrtash Babadi, Rex Ying, and Wengong Jin. Stpath: a generative foundation model for integrating spatial transcriptomics and whole-slide images. *NPJ Digital Medicine*, 8(1):659, 2025.
54. Yuequn Wang, Jun Wang, Yanyu Xu, Ning Liu, Bin Liu, Yuliang Li, and Guoxian Yu. Fmh2st: foundation model-based spatial transcriptomics generation from histological images. *Nucleic Acids Research*, 53(17):gkaf865, 2025.
55. Musu Yuan, Kaitian Jin, Hanying Yan, Amelia Schroeder, Chunyu Luo, Sicong Yao, Bernhard Dumoulin, Jonathan Levinsohn, Tianhao Luo, Jean R Clemenceau, et al. Smart spatial omics (s2-omics) optimizes region of interest selection to capture molecular heterogeneity in diverse tissues. *Nature cell biology*, pages 1–14, 2025.
56. Ron Zeira, Max Land, Alexander Strzalkowski, and Benjamin J. Raphael. Alignment and

integration of spatial transcriptomics data. *Nature Methods*, 19(5):567–575, 2022. doi: 10.1038/s41592-022-01459-6.

57. Andrew Jones, F. William Townes, Didong Li, and Barbara E. Engelhardt. Alignment of spatial genomics data using deep gaussian processes. *Nature Methods*, 20(9):1379–1387, 2023. doi: 10.1038/s41592-023-01972-2.